

A stripe phase with supersolid properties in spin–orbit–coupled Bose–Einstein condensates

Jun-Ru Li^{1*}, Jeongwon Lee^{1*}, Wujie Huang¹, Sean Burchesky¹, Boris Shteynas¹, Furkan Çağrı Top¹, Alan O. Jamison¹ & Wolfgang Ketterle¹

Supersolidity combines superfluid flow with long-range spatial periodicity of solids¹, two properties that are often mutually exclusive. The original discussion of quantum crystals² and supersolidity focused on solid ⁴He and triggered extensive experimental efforts^{3,4} that, instead of supersolidity, revealed exotic phenomena including quantum plasticity and mass supertransport⁴. The concept of supersolidity was then generalized from quantum crystals to other superfluid systems that break continuous translational symmetry. Bose–Einstein condensates with spin–orbit coupling are predicted to possess a stripe phase^{5–7} with supersolid properties^{8,9}. Despite several recent studies of the miscibility of the spin components of such a condensate^{10–12}, the presence of stripes has not been detected. Here we observe the predicted density modulation of this stripe phase using Bragg reflection (which provides evidence for spontaneous long-range order in one direction) while maintaining a sharp momentum distribution (the hallmark of superfluid Bose–Einstein condensates). Our work thus establishes a system with continuous symmetry-breaking properties, associated collective excitations and superfluid behaviour.

Supersolids are defined as systems that spontaneously break two continuous U(1) symmetries: the global phase of the superfluid breaks the internal gauge symmetry, and a density modulation breaks the translational symmetry of space. Starting from superfluid Bose–Einstein condensates (BECs), several forms of supersolidity have been predicted to occur when the condensates feature dipolar interactions¹³, Rydberg interactions¹⁴, superradiant Rayleigh scattering¹⁵, nearest-neighbour interaction in lattices¹⁶ or spin–orbit interactions^{5–7}. Work simultaneous with ours used light scattering into two cavities to realize a BEC with supersolid properties¹⁷. For fermions, the predicted Fulde–Ferrell–Larkin–Ovchinnikov states have supersolid properties^{18,19}. Several of these proposals lead to solidity along a single spatial direction maintaining gaseous or liquid-like properties along the other directions. These systems are different from quantum crystals, but share the symmetry-breaking properties.

Spin–orbit coupling occurs in solid-state materials when an electron moving at velocity \mathbf{v} through an electric field \mathbf{E} experiences a Zeeman energy term $-\mu_B \boldsymbol{\sigma} \cdot (\mathbf{v} \times \mathbf{E})$ owing to the relativistic transformation of electromagnetic fields. Here $\boldsymbol{\sigma}$ is the spin vector and μ_B is the Bohr magneton. The Zeeman term can be written as $\alpha_{ij} v_j \sigma_i / 4$, where the strength of the coupling α has the units of momentum. The $v_x \sigma_z$ term, together with the transverse magnetic Zeeman term $\beta \sigma_x$, leads to the Hamiltonian $H = ((P_x + \alpha \sigma_z)^2 + P_y^2 + P_z^2) / 2m + \beta \sigma_x$, where m is the atomic mass. A unitary transformation can shift the momenta by $\alpha \sigma_z$, resulting in

$$H = \frac{P^2}{2m} + \begin{pmatrix} 0 & \beta e^{2i\alpha x} \\ \beta e^{-2i\alpha x} & 0 \end{pmatrix} \quad (1)$$

The second term represents a spin-flip process with a momentum transfer of 2α , which is therefore equivalent to a form of spin–orbit

coupling. Such a spin-flip process can be directly implemented for ultracold atoms using a two-photon Raman transition between the two spin states^{10,20}.

Without spin–orbit coupling, a BEC populating two spin states shows no spatial interference, owing to the orthogonality of the states. With spin–orbit coupling, each spin component has now two momentum components (0 and either $+2\alpha$ or -2α , where the sign depends on the initial spin state), which form a stationary spatial interference pattern with a wavevector of 2α (Fig. 1a). Such spatial periodicity of the atomic density can be directly probed with Bragg scattering²¹, as shown in Fig. 1b. The position of the stripes is determined by the relative phase of the two condensates. This spontaneous phase breaks continuous translational symmetry. The two broken U(1) symmetries are reflected in two long-wavelength collective excitations (the Goldstone modes), one for density (or charge), the other one for spin transport⁹. Adding a longitudinal Zeeman term $\delta_0 \sigma_z$ to equation (1) leads to a rich phase diagram^{6,22} as a function of δ_0 and β . For sufficiently large $|\delta_0|$, the ground state is in a plane-wave phase. This phase has a roton gap^{9,11}, which decreases when $|\delta_0|$ is reduced, causing a roton instability and leading to a phase transition into the stripe phase.

Most experimental studies of spin–orbit coupling with ultracold atoms used two hyperfine ground states coupled by a two-photon Raman spin-flip process^{10–12,23–26}. So far direct evidence of the spatial modulation pattern has been missing, possibly suppressed by stray magnetic fields detuning the Raman transitions and low miscibility between the hyperfine states used (see Methods). Both limitations were recently addressed by a new spin–orbit coupling scheme in which orbital states (the lowest two eigenstates in an asymmetric double-well potential) are used as the pseudospins²⁷. Since the eigenstates mainly populate different wells, their interaction strength g_{\perp} is small and can be adjusted by adjusting their spatial overlap, improving the miscibility (see Methods). Furthermore, since both pseudospin states have the same hyperfine state, there is no sensitivity to magnetic fields. The scheme is realized with a coherently coupled array of double wells using an optical superlattice, a periodic structure with two lattice sites per unit cell with intersite tunnelling J (Fig. 2a). The superlattice has two low-lying bands, split by the energy difference Δ between the double wells, each hosting a BEC in the respective band minima. The BECs in the lower and upper band minima are the pseudospin states in our system. Spin–orbit coupling and the supersolid stripes are created for the free-space motion in the two-dimensional plane orthogonal to the superlattice. The physics in a single two-dimensional plane is not modified in a stack of coherently coupled double wells. However, this increases the signal-to-noise ratio and suppresses the background to the Bragg signal (see below).

Experiments started with approximately 1×10^{23} Na atoms forming a BEC loaded into the optical superlattice along the z direction, equally split between the two pseudospin states with a density $n \approx 1.5 \times 10^{14} \text{ cm}^{-3}$. The superlattice consists of laser beams at

¹Department of Physics, MIT-Harvard Center for Ultracold Atoms, and Research Laboratory of Electronics, MIT, Cambridge, Massachusetts 02139, USA.

*These authors contributed equally to this work.

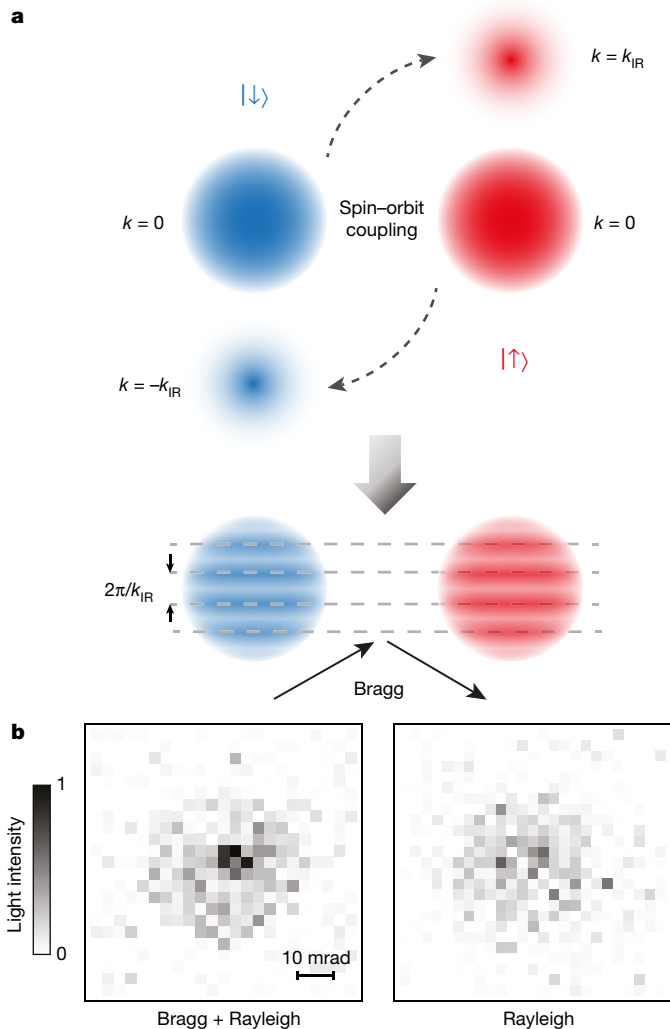


Figure 1 | Origin of supersolid stripes and detection via Bragg scattering. **a**, Supersolid stripes from spin-orbit coupling. Spin-orbit coupling adds momentum components $+\hbar k_{\text{IR}}$ or $-\hbar k_{\text{IR}}$ of the opposite spin state to the spin-up and spin-down BECs (at the top are spin states in momentum space). Matter wave interference leads to a spatial density modulation of period $2\pi/k_{\text{IR}}$ (at the bottom are spin states in real space). The spatial periodicity can be directly probed by Bragg scattering. **b**, Angle-resolved Bragg signal. The supersolid stripe phase is detected by angle-resolved light scattering. A sharp specular feature in the left panel is the Bragg signal due to the periodic density modulation. The diffuse signal is Rayleigh scattering filling the round aperture of the imaging system. Without spin-orbit coupling, only Rayleigh scattering is observed (right panel). The figure is the average over seven shots.

wavelengths of 1,064 nm and 532 nm, resulting in a lattice constant of $d = 532$ nm. Spin-orbit coupling was induced by two infrared (IR) Raman laser beams $\lambda_{\text{IR}} = 1,064$ nm along the x and z axes, providing a momentum transfer $\hbar \mathbf{k}_{\text{Raman}} = \hbar(k_{\text{IR}}, 0, k_{\text{IR}})$ and spin flip from one well to the other with two-photon Rabi frequency Ω . Here $\hbar k_{\text{IR}} = 2\pi\hbar/\lambda_{\text{IR}}$ is the recoil momentum from a single infrared photon (see ref. 27 and Methods). The scheme realizes the spin-orbit Hamiltonian in equation (1) with $\alpha = k_{\text{IR}}/2$, $\beta = (1/\sqrt{2})J\Omega/\Delta$, and an extra Zeeman term $\delta_0\sigma_z = (\delta - \Delta)/2\sigma_z$, depending on the Raman-beam detuning δ and the superlattice offset Δ . The parameters J , Ω and Δ are determined from calibration experiments²⁷. A separate laser beam was added in the x - y plane to enable detection of the stripes, which form perpendicularly to the superlattice with a periodicity of approximately $2d = 1,064$ nm. Their detection requires near-resonant yellow light (Bragg probe light wavelength $\lambda_{\text{Bragg}} = 589$ nm) at an incident angle $\theta = 16^\circ$, fulfilling the Bragg condition $\lambda_{\text{Bragg}} = 4d\sin\theta$.

Figure 1b shows the angular distribution of the Rayleigh-scattered light induced by the 589-nm laser at $\delta_0 = 0$ in the Bragg direction (see Methods). The spin-orbit coupling leads to supersolid stripes and causes a specular reflection of the Bragg beam, observed as a sharp feature in the angular distribution of the Rayleigh-scattered light (Fig. 1b). The angular width (full-width at half-maximum, FWHM) of the observed peak of 9 ± 1 mrad is consistent with the diffraction limit of λ_{Bragg}/D , where D is the FWHM size of the cloud, demonstrating phase coherence of the stripes throughout the whole cloud. This observation of the Bragg-reflected beam is our main result, and constitutes a direct observation of the stripe phase with long-range order. For the same parameters, we observe sharp momentum peaks in time of flight²⁷—the signature of BECs—which implies superfluidity.

Our detection of the stripe phase is almost background-free, since all other density modulations have different directions, as depicted in Fig. 2a. The superlattice is orthogonal to the stripes, along the z axis. The Raman beams form a moving lattice and create a propagating density modulation at an angle of 45° to the superlattice, parallel to $\hat{x} + \hat{z}$. The pseudospin state in the upper band of the superlattice forms at the minimum of the band at a quasimomentum of $q = \pi/d$. The wavevector of the stripes is the sum of this quasimomentum and the momentum transfer that accompanies the spin-flip of the spin-orbit coupling interaction²⁷, resulting in a stripe wavevector in the x direction. Since the difference in the wavevectors between the off-resonant density modulation and the stripes is not a reciprocal lattice vector, the Bragg condition cannot be simultaneously fulfilled for both density modulations. This background-free Bragg detection of the stripes uniquely depends on the realization of a coherent array of planar spin-orbit-coupled systems.

For a pure condensate, the contrast of the density modulation is predicted^{5,6} to be $\eta = 2\beta/E_r$, which is about 8% for $\beta \approx 300$ Hz. Here $E_r = 7.6$ kHz is the ^{23}Na recoil energy for a single 1,064-nm photon. A sinusoidal density modulation of ηN_{BEC} (where N_{BEC} is the number of atoms in the BEC) atoms gives rise to a Bragg signal equivalent to $\gamma(\eta N_{\text{BEC}})^2/4$, where γ is the independently measured Rayleigh scattering signal per atom per solid angle, and the factor $1/4$ is the Debye-Waller factor for a sinusoidal modulation. In Fig. 2b, we observed the expected behaviour of the Bragg signal to be proportional to N_{BEC}^2 with the appropriate pre-factors. The prediction for the signal assumes that the stripes are long-range-ordered throughout the whole cloud. If there were m domains, the signal would be m times smaller. Therefore, the observed strength of the Bragg signals confirms the long-range coherence already implied by the sharpness of the angular Bragg peak. Another way to quantify the Bragg signal is to define the ratio of the peak Bragg intensity to the Rayleigh intensity as ‘gain’, which is calculated to be $N_{\text{total}}(f\beta/E_r)^2$, where $f = N_{\text{BEC}}/N_{\text{total}}$ is the condensate fraction. The inset of Fig. 2b shows the normalized gain as a function of condensate fraction squared. The linear fit to the data points is consistent with a y -axis intercept of zero. This shows that the observed gain comes only from the superfluid component of the atomic sample. Figure 2c shows that the Bragg signal increases with larger spin-orbit-coupling strength up to $\beta \approx 300$ Hz, and starts to decrease owing to heating from the Raman driving (see Methods).

Figure 3a shows the phase diagram for spin-orbit-coupled BECs for the parameters implemented in this work. The stripe phase is wide, owing to the high miscibility of the two orbital pseudospin states. Our spin-orbit coupling scheme and the one previously used^{10,11} with ^{87}Rb are complementary. In ^{87}Rb , the phase-separated and the single-minimum states were easily observed^{10,11}, whereas our scheme favours the stripe phase.

Exploring the phase diagram in the vertical direction requires varying δ_0 with the two Raman beams detuned. For $\delta_0 = 0$, spin-orbit coupling leads to two degenerate spin states. For sufficiently large values of $|\delta_0|$, the ground state is the lower spin state. The vertical width of the stripe phase in Fig. 3a depends on the miscibility of the two spin components^{6,22}. However, population relaxation between the two spin states is very slow¹⁰. For our parameters, the equal population of the two pseudospin states is constant during the lifetime of the system for

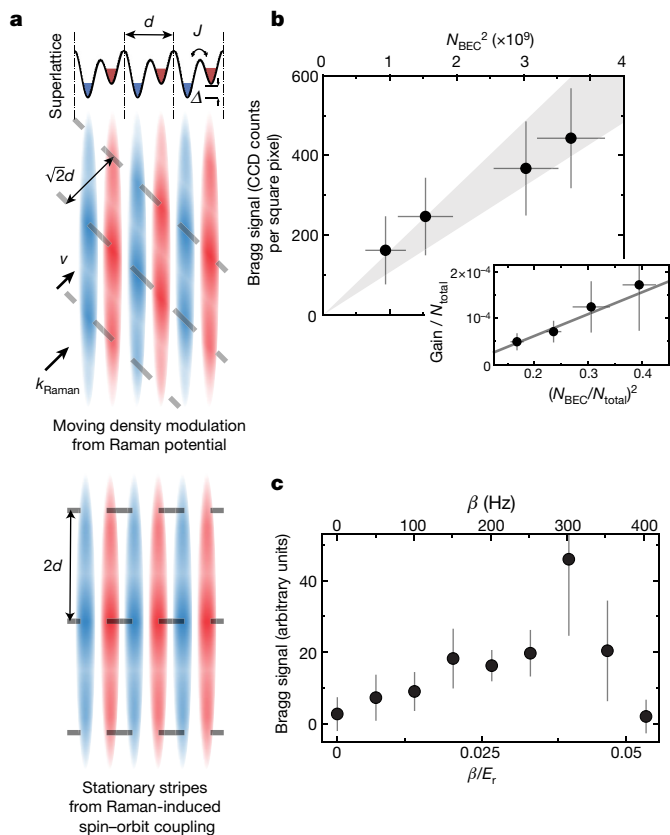


Figure 2 | Density modulations from Raman beams, and quantitative studies of the supersolid stripes. **a**, Effect of Raman beams. The two lowest bands of the superlattice are mapped into orbital pseudospins, where the pseudospin down state (localized in the left wells of the superlattice) is shown in blue and the pseudospin up state (localized in the right wells of the superlattice) is shown in red. Coupling the pseudospins with Raman laser beams causes two different types of density modulations; one is a moving density modulation caused by the moving lattice potential, and the other is the stationary stripes from Raman-induced spin-orbit coupling between the pseudospins. The stationary stripes along the free-space x direction break the continuous translational symmetry. **b**, BEC number dependence. Bragg signal is plotted versus the BEC number, showing the count rate integrated over the Bragg peak. The grey wedge is the theoretical prediction without any adjustable parameters, using independently measured values of β and γ (and the corresponding 1σ errors) along with the theoretical Debye–Waller factor, assuming full phase coherence of the stripes. The simple theory (see main text) predicts the peak angular amplitude of the Bragg signal. To compare it to the total count rate, we assumed a Gaussian lineshape with a constant linewidth. The linewidth was obtained by averaging the widths obtained from two-dimensional Gaussian fits to the data for each condensate number. The inset shows the normalized gain as the BEC fraction is varied. The grey solid line is a linear fit, where the y -axis intercept is consistent with zero, within 2σ fitting error. **c**, Spin-orbit-coupling dependence. Bragg signal versus Raman coupling strength β at zero Raman detuning is shown. Error bars represent 1σ standard error of the mean with a sample size of 3 to 4.

all detunings $|\delta_0|$ studied (up to ± 10 kHz). Therefore, detection of the stripes is possible even for large detuning.

We observed peaked Bragg reflection at $\delta_0 \approx \pm 0.7E_r$, which was characterized previously as spin-flip resonances coupling $|\uparrow, P=0\rangle$ to $|\downarrow, P=-\hbar k_{\text{IR}}\rangle$ and $|\downarrow, P=0\rangle$ to $|\uparrow, P=-\hbar k_{\text{IR}}\rangle$ (Fig. 3b). These peaks show that density modulations are resonantly created in either the $|\uparrow\rangle$ or $|\downarrow\rangle$ states. In addition, we observed a third peak around $\delta_0 = 0$, where the stripe pattern is stationary. For finite δ_0 , it moves at a velocity of δ_0/k_{IR} . Our observation shows that the stationary stripe pattern is either more stable or has higher contrast compared to a moving stripe. Since the tunnel coupling along the superlattice direction is weak (about 1 kHz) it seems possible that the alignment of moving stripe patterns

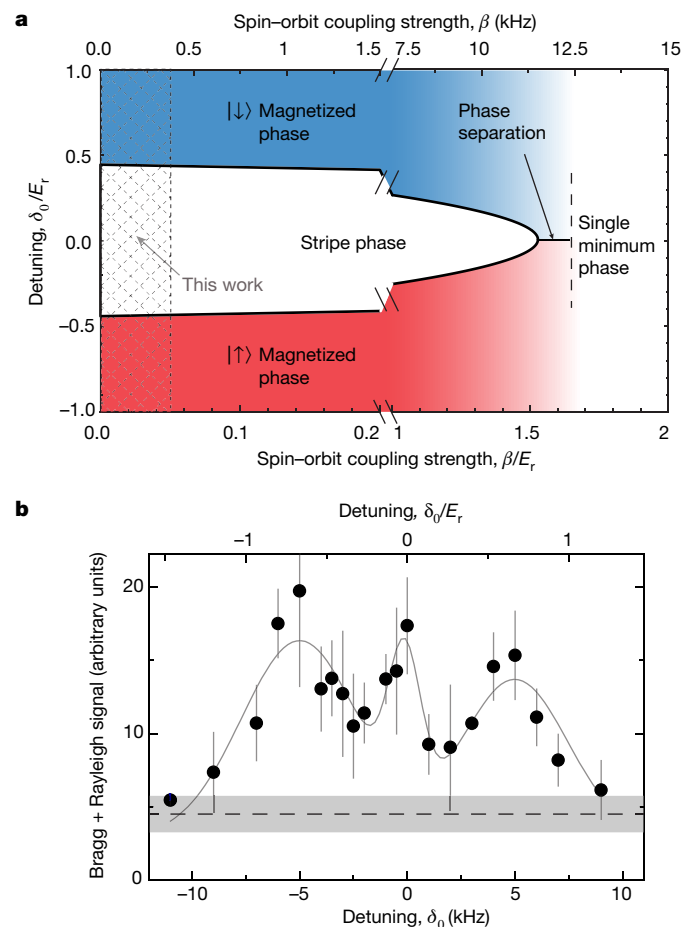


Figure 3 | Phase diagram for spin-orbit-coupled BECs, and effect of Raman detuning on the supersolid stripes. **a**, Mean-field phase diagram of spin-orbit-coupled BECs as a function of detuning and spin-orbit-coupling strength with $n \approx 1.5 \times 10^{14} \text{ cm}^{-3}$. The parameter space explored in this work is crosshatched in grey. However, owing to metastability, our effective detuning is always zero (see text). **b**, Detuning dependence. Black filled circles show the total light scattering signal (Bragg and Rayleigh) as a function of the frequency detuning. The light was detected within a solid angle of 10 mrad. The grey dashed line and shaded area show the mean and standard deviation of the Rayleigh scattered light for the same conditions. The light-grey solid line is a triple Gaussian fit to the total light scattering where the widths and centre positions of the two outer peaks are constrained to be identical to the spin-flip resonances studied in our previous work²⁷. Error bars represent 1σ standard error of the mean with a sample size of 3 to 6.

is more sensitive to perturbations than for stationary stripes and leads to a reduced Debye–Waller factor for moving stripes.

The periodicity of the supersolid density modulation can depend on external, single-atom, and two-atom parameters. In the present case, the periodicity is given by the wavelength and geometry of the Raman beams. It is then further modified by the spin gap parameter β and the interatomic interactions^{5,6} to become $2d/\sqrt{1-(\beta/F)^2}$, where $F = (2E_r + n(g+g_{\perp}))/4$. For $\beta \approx 300$ Hz, the correction due to the interactions is only 0.4% and was not detected in our work. In contrast, for the dipolar supersolid¹³ and a quantum crystal with vacancies^{1,2}, the periodicity dominantly depends on atomic interactions.

So far, we have presented a supersolid that breaks the continuous translational symmetry in the free-space x direction (Fig. 2a). Unrelated to the presence of spin-orbit coupling, our superlattice system also breaks a discrete translational symmetry along the lattice direction \hat{z} by forming a spatial period that is twice that of the external lattice owing to the interference between atoms in the two pseudospin states with quasimomentum difference $\Delta q = \pi/d$ (Fig. 4a) (see ref. 27). This fulfils the definition of a lattice supersolid^{19,28}. This 1,064-nm-period

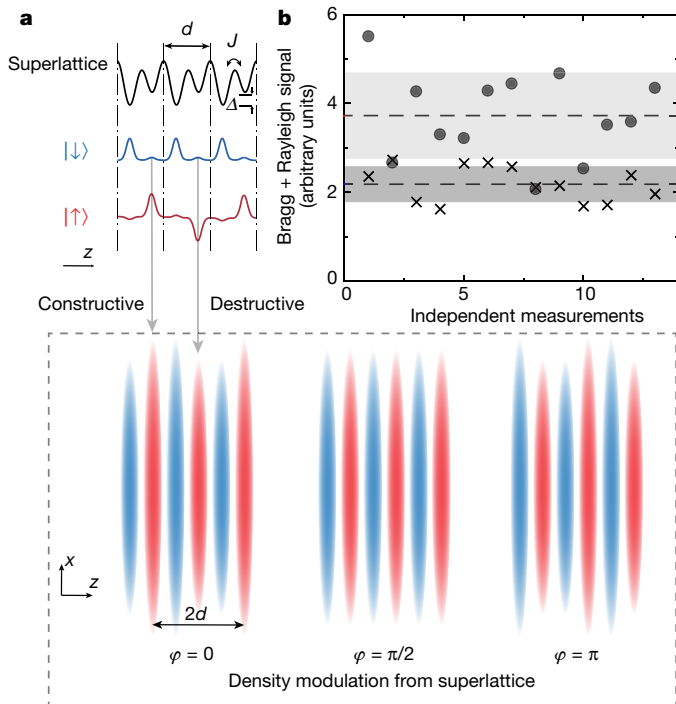


Figure 4 | Bragg detection of a lattice supersolid caused by an antiferromagnetic spin texture. **a**, Phase-sensitive density modulation of the lattice supersolid. The interference between the pseudospin down and up states alternates between constructive and destructive for adjacent unit cells in the lattice. This generates an oscillating density modulation, which has a spatial periodicity of $2d$ along the superlattice direction \hat{z} and depends on the relative phases between the orbital pseudospins as $\varphi = \varphi_0 + \Delta t$, with φ_0 as the spontaneous phase. The density modulations at different phase conditions are shown below (in the dashed box). This breaks the discrete symmetry of the lattice potential. **b**, The Bragg signal for independent measurements with $n \approx 1.5 \times 10^{14} \text{ cm}^{-3}$. The Bragg signal, which is set up for detection of a spatial periodicity of $2d$ along the superlattice, depends on the relative phase φ when the Bragg pulse width is shorter than $1/(2\Delta)$. Black crosses show the Rayleigh-scattered background integrated over 40 mrad before the antiferromagnetic spin texture develops. Grey filled circles show Bragg-enhanced scattering. The Bragg enhancement fluctuated between zero and a factor of two, which indicates variations of the spontaneous phase φ_0 between independent measurements.

density modulation has a maximum amplitude of (J/Δ) and oscillates at frequency 2Δ temporally with spontaneous initial phase and can be detected with the same geometry of the Bragg beam and camera, but rotated to the y - z plane. Figure 4b shows the observed enhanced light scattering due to Bragg reflection. The enhancement was absent immediately after preparing an equal mixture of the two pseudospin states, both in $q = 0$, and appeared spontaneously after the upper pseudospin state relaxed to the band minimum at $q = \pi/d$. With the Bragg pulse duration shorter than $1/(2\Delta)$, the Bragg signal varied between 0% and 100%, depending on the phase of the oscillation of the density modulation when probed. The increased fluctuation in Fig. 4b shows the random nature of the initial phase, which is consistent with spontaneous symmetry breaking.

In conclusion, we have observed the long-predicted supersolid stripe phase of spin-orbit-coupled BECs. This realizes a system that simultaneously has off-diagonal and diagonal long-range order. In the future, it will be interesting to characterize this system's collective excitations⁹ and to find ways to extend it to two-dimensional spin-orbit coupling, which leads to a different and rich phase diagram²⁹. Another direction for future research is the study of vortices and the effects of impurities and disorder in different phases of spin-orbit-coupled condensates³⁰.

Online Content Methods, along with any additional Extended Data display items and Source Data, are available in the online version of the paper; references unique to these sections appear only in the online paper.

Received 26 October 2016; accepted 14 January 2017.

- Boninsegni, M. & Prokof'ev, N. V. Supersolids: what and where are they? *Rev. Mod. Phys.* **84**, 759–776 (2012).
- Chester, G. V. Speculations on Bose–Einstein condensation and quantum crystals. *Phys. Rev. A* **2**, 256–258 (1970).
- Kim, E. & Chan, M. H. W. Probable observation of a supersolid helium phase. *Nature* **427**, 225–227 (2004).
- Kuklov, A. B., Pollet, L., Prokof'ev, N. V. & Svistunov, B. V. Quantum plasticity and supersolid response in helium-4. *Phys. Rev. B* **90**, 184508 (2014).
- Li, Y., Pitaevskii, L. P. & Stringari, S. Quantum tricriticality and phase transitions in spin-orbit-coupled Bose–Einstein condensates. *Phys. Rev. Lett.* **108**, 225301 (2012).
- Ho, T.-L. & Zhang, S. Bose–Einstein condensates with spin-orbit interaction. *Phys. Rev. Lett.* **107**, 150403 (2011).
- Wang, C., Gao, C., Jian, C.-M. & Zhai, H. Spin-orbit coupled spinor Bose–Einstein condensates. *Phys. Rev. Lett.* **105**, 160403 (2010).
- Han, W., Juzeliūnas, G., Zhang, W. & Liu, W.-M. Supersolid with nontrivial topological spin textures in spin-orbit-coupled Bose gases. *Phys. Rev. A* **91**, 013607 (2015).
- Li, Y., Martone, G. I., Pitaevskii, L. P. & Stringari, S. Superstripes and the excitation spectrum of a spin-orbit-coupled Bose–Einstein condensate. *Phys. Rev. Lett.* **110**, 235302 (2013).
- Lin, Y.-J., Jiménez-García, K. & Spielman, I. B. Spin-orbit-coupled Bose–Einstein condensates. *Nature* **471**, 83–86 (2011).
- Ji, S.-C. *et al.* Softening of roton and phonon modes in a Bose–Einstein condensate with spin-orbit coupling. *Phys. Rev. Lett.* **114**, 105301 (2015).
- Ji, S.-C. *et al.* Experimental determination of the finite-temperature phase diagram of a spin-orbit coupled Bose gas. *Nat. Phys.* **10**, 314–320 (2014).
- Giovanazzi, S., O'Dell, D. & Kurizki, G. Density modulations of Bose–Einstein condensates via laser-induced interactions. *Phys. Rev. Lett.* **88**, 130402 (2002).
- Henkel, N., Nath, R. & Pohl, T. Three-dimensional roton excitations and supersolid formation in Rydberg-excited Bose–Einstein condensates. *Phys. Rev. Lett.* **104**, 195302 (2010).
- Ostermann, S., Piazza, F. & Ritsch, H. Spontaneous crystallization of light and ultracold atoms. *Phys. Rev. X* **6**, 021026 (2016).
- Wessel, S. & Troyer, M. Supersolid hard-core bosons on the triangular lattice. *Phys. Rev. Lett.* **95**, 127205 (2005).
- Léonard, J. *et al.* Supersolid formation in a quantum gas breaking a continuous translational symmetry. *Nature* <http://dx.doi.org/10.1038/nature21067> (2017).
- Bulgac, A. & Forbes, M. M. Unitary Fermi supersolid: the Larkin–Ovchinnikov phase. *Phys. Rev. Lett.* **101**, 215301 (2008).
- Chen, Y., Ye, J. & Tian, G. Classification of a supersolid: trial wavefunctions, symmetry breaking and excitation spectra. *J. Low Temp. Phys.* **169**, 149–168 (2012).
- Stanescu, T. D., Anderson, B. & Galitski, V. Spin-orbit coupled Bose–Einstein condensates. *Phys. Rev. A* **78**, 023616 (2008).
- Miyake, H. *et al.* Bragg scattering as a probe of atomic wave functions and quantum phase transitions in optical lattices. *Phys. Rev. Lett.* **107**, 175302 (2011).
- Martone, G. I. Visibility and stability of superstripes in a spin-orbit-coupled Bose–Einstein condensate. *Eur. Phys. J. Spec. Top.* **224**, 553–563 (2015).
- Burdick, N. Q., Tang, Y. & Lev, B. Long-lived spin-orbit-coupled degenerate dipolar Fermi gas. *Phys. Rev. X* **6**, 031022 (2016).
- Cheuk, L. W. *et al.* Spin-injection spectroscopy of a spin-orbit coupled Fermi gas. *Phys. Rev. Lett.* **109**, 095302 (2012).
- Wang, P. *et al.* Spin-orbit coupled degenerate Fermi gases. *Phys. Rev. Lett.* **109**, 095301 (2012).
- Song, B. *et al.* Spin-orbit coupled two-electron Fermi gases of ytterbium atoms. *Phys. Rev. A* **94**, 061604(R) (2016).
- Li, J. *et al.* Spin-orbit coupling and spin textures in optical superlattices. *Phys. Rev. Lett.* **117**, 185301 (2016).
- Baumann, K., Guerlin, C., Brennecke, F. & Esslinger, T. Dicke quantum phase transition with a superfluid gas in an optical cavity. *Nature* **464**, 1301–1306 (2010).
- Sun, Q., Wen, L., Liu, W.-M., Juzeliūnas, G. & Ji, A.-C. Tunneling-assisted spin-orbit coupling in bilayer Bose–Einstein condensates. *Phys. Rev. A* **91**, 033619 (2015).
- Zhai, H. Degenerate quantum gases with spin-orbit coupling. *Rep. Prog. Phys.* **78**, 026001 (2015).

Acknowledgements We thank S. Stringari for discussions and W. C. Burton for reading the manuscript. We acknowledge support from the NSF through the Center for Ultracold Atoms and from award 1506369, from ARO-MURI Non-equilibrium Many-body Dynamics (grant W911NF-14-1-0003) and from AFOSR-MURI Quantum Phases of Matter (grant FA9550-14-1-0035).

Author Contributions J.-R.L., W.H., J.L., B.S., S.B., F.C.T. and A.O.J. contributed to the building of the experiment. J.-R.L. led the experimental efforts. J.L. led the data analysis and simulations. W.H., J.-R.L. and W.K. conceived the experiment. All authors contributed to the writing of the manuscript.

Author Information Reprints and permissions information is available at www.nature.com/reprints. The authors declare no competing financial interests. Readers are welcome to comment on the online version of the paper. Correspondence and requests for materials should be addressed to J.-R.L. (junruli@mit.edu).

Reviewer Information *Nature* thanks K. Hazzard and the other anonymous reviewer(s) for their contribution to the peer review of this work.

METHODS

Experimental setup and sample preparation. The superlattice (SL) potential $V(z) = V_{\text{IR}} \sin^2(k_{\text{IR}}z + \phi_{\text{SL}}) + V_{\text{Green}} \sin^2(k_{\text{Green}}z)$ was generated by overlapping two one-dimensional lattices with spacing $\lambda_{\text{IR}}/2 = 532$ nm (long) and $\lambda_{\text{Green}}/2 = 266$ nm (short). The relative phase ϕ_{SL} is controlled by the frequency of the 1,064-nm lattice light for rapid switching and a rotatable dispersive glass plate in the lattice beam path. The offset Δ is determined by V_{IR} and ϕ_{SL} and is calibrated by observing the oscillation of the interference pattern between atoms released from the two wells²⁷. We estimate the fluctuations of the offset parameter Δ to be within 1 kHz, caused by drifts in the air pressure that affect the relative phase ϕ_{SL} between the two lattices.

The two Raman beams were generated from the same laser and then split into two parts. The relative frequency was tuned by two independent acousto-optic modulators in each path. We prepared $N \approx 4 \times 10^5$ Na atoms in a crossed optical dipole trap. An equal mixture of spin-up and spin-down states was created by first adiabatically ramping up the superlattice with an offset $\Delta = 0$ and then rapidly setting Δ to the final value by a fast frequency change of the infrared lattice²⁷. Subsequently, the Raman lasers inducing the spin-orbit coupling are adiabatically ramped up within about 10 ms followed by a variable hold time, after which the Bragg probe beam is applied.

Miscibility and the stripe phase. Achieving stable and high-contrast stripes requires miscibility of the two spin components. The difference in energy density between a BEC in the stripe phase and a phase-separated phase is $g\delta n^2 - (g - g_{\perp})n^2$ where $g = 4\pi\hbar^2 a/m$ and $g_{\perp} = 4\pi\hbar^2 a_{\perp}/m$ parameterize the interaction energy strengths between atoms in the same and in different spin states, respectively. Here a (a_{\perp}) is the interspin (intraspin) s -wave scattering length. The extra mean-field energy due to a modulation of the density n with amplitude δn leads to phase separation when the contrast of the stripes $\eta = \delta n/n$ exceeds $\sqrt{(g - g_{\perp})/g}$. All previous studies with bosons used ⁸⁷Rb atoms^{10–12}. For ⁸⁷Rb atoms in the $|F = 1, m_F = 0\rangle$ and $|F = 1, m_F = -1\rangle$ states, $(g - g_{\perp})/g = 10^{-3}$ is extremely small. In addition, the full width in δ_0 for stable stripes is $W = 2n(g - g_{\perp})$, which is about 10 Hz for ⁸⁷Rb and requires extreme control of ambient magnetic field fluctuations. For these reasons the stripe phase has not yet been observed in previous studies of spin-orbit-coupled rubidium atoms^{10–12}.

Using the orbital degree of freedom as pseudospin, Raman lights can be far-detuned from atomic transitions, suppressing spontaneous emission heating. In addition, the orbital overlap controls the intra-spin interaction $g_{\perp} \approx (J/\Delta)g$, where J is the

interwell tunnelling and Δ is the well offset²⁷. For typical experimental parameters with $(J/\Delta) \approx 1/20$, $(g - g_{\perp})/g \approx 1$. The highly imbalanced interaction enhances the miscibility and therefore allows higher contrast and more stable stripes.

Bragg beam parameters and detection. The Bragg beam was chosen to be blue-detuned about 1,030 MHz from the sodium $|3S_{1/2}, F = 1\rangle$ to $|3P_{3/2}, F = 2\rangle$ transition with a linear polarization along the superlattice direction. The detuning was chosen such that the Bragg beam can propagate through the entire condensate without much absorption or wave-front distortion.

The alignment of the Bragg beam required accurate prealignment by triangulation. A major challenge was the alignment of this beam to an accuracy of better than about 0.5°, the angular width of the Bragg signal, without any auxiliary density modulation at the same periodicity, given that creating such a density modulation would have required a standing wave of laser light at 2,128 nm. Experimentally, the lattice supersolid is more robust than the stripe phase while having the same periodicity of the density modulation. Therefore, the alignment procedure was first developed for the lattice supersolid. The same setting was rotated around the axis \hat{y} by 90° to probe for the stripe phase.

The Bragg reflected beam and the Rayleigh fluorescence were recorded with an electron multiplying charge-coupled device (CCD) camera. The angular distribution was recorded by first focusing an imaging system onto the camera and then moving the camera out of focus. The signal was normalized for fluctuating atom numbers using the fluorescence intensity monitored by a photomultiplier using a separate viewport. The Bragg signal was obtained by integrating the counts of the CCD pixels around the Bragg-matched angle. The Rayleigh signal was obtained from fitting the diffuse background with a two-dimensional Gaussian fit. The detected Bragg signal was of the order of only ten photons.

We observed a lifetime of about 20 ms for the Bragg signal after ramping up the spin-orbit coupling, accompanied by a clearly visible reduction in the number of atoms in the BEC. We believe that it is limited by the heating due to the Raman driving²⁷. At values of $\beta \approx 300$ Hz, the moving Raman lattice has a depth of about $3E_r$, which is comparable to the stationary lattice at around $10E_r$. When the spin-orbit coupling was increased further, the Bragg signal decreased, as shown in Fig. 2c, with noticeable atom loss. In addition, the observed heating may still have a contribution from technical sources, since the observed lifetime is sensitive to alignment.

Data availability. The data that support the findings of this study are available from the corresponding author upon reasonable request.